EES Batteries

Accepted Manuscript

This article can be cited before page numbers have been issued, to do this please use: M. Nasir, J. Seo, S. I. Jung and H. J. Park, *EES Batteries*, 2025, DOI: 10.1039/D5EB00026B.

View Article Online
DOI: 10.1039/D5EB00026B

Liquid Electrolyte-Assisted Stabilization of the LLZO/Li Interface for Stable Lithium Metal Batteries

*Mohammad Nasir[1,2], Jun Seo[1], Seo In Jung[1], and Hee Jung Park[1,2,3]**

[1]*Department of Materials Science and Engineering, Dankook University, Cheonan, 31116, Republic of Korea*

[2]*Hydrogen Research Center, Dankook University, Cheonan, 31116, Republic of Korea*

[3]*Department of Materials Science and Engineering, University of Washington, Seattle, WA, USA*

**Corresponding author's email address: parkjang@dankook.ac.kr (Hee Jung Park)*

ABSTRACT

Garnet-based solid-state batteries offer high energy density and improved safety but face challenges such as poor interfacial compatibility and high resistance at the LLZO/Li interface due to their lithiophobic nature. To address these issues, we applied a small amount of carbonate and ether-based liquid electrolytes to wet the surface of $La_{6.25}Ga_{0.25}La_3ZrO_{12}$ (LLZO) pellets, enhancing wettability and reducing interfacial resistance. Cubic phase LLZO with a dense microstructure demonstrated excellent ionic conductivity of 1.53 mS/cm and a low activation energy of 0.268 eV, enabling efficient Li-ion transport. Symmetric cell studies revealed superior performance with ether-based electrolytes due to the formation of Li_3N/LiF rich interphase, achieving significantly lower interfacial resistance (~32 Ω·cm^2) and a higher critical current density (0.6 mA/cm^2) compared to carbonate-based systems. Long-term cycling tests confirmed stability of ether-based cells, maintaining over 1000 h of stable cycling at 0.1 mA/cm^2. Full cells with $LiFePO_4$ (LFP) cathodes demonstrated excellent compatibility, retaining 78.5% capacity after 100 cycles with 99.9% Coulombic efficiency. These results underscore the potential of minimal liquid electrolyte usage as a scalable and cost effective strategy to optimize the LLZO/Li interface for hybrid solid-state batteries.

Keywords: Zero Li-excess, Li-ion conductivity, Solid electrolyte, Interfacial resistance, All solid-state batteries

View Article Online
DOI: 10.1039/D5EB00026B

Broader context

The transition to sustainable energy demands advanced storage solutions like lithium metal and solid-state batteries, which offer high energy density and improved safety but face challenges such as interfacial resistance and dendrite formation. Garnet-based solid electrolytes like LLZO show promise due to their high ionic conductivity and stability, yet their lithiophobic nature hinders lithium compatibility. While strategies such as metallic coatings and chemical treatments address interfacial issues, they often lack scalability. In response to these challenges, we explore the use of minimal liquid electrolytes to enhance LLZO/Li interface wettability, reducing resistance, improving Li-ion transport, and suppressing dendrites. This scalable and cost effective approach aligns with broader advancements in material design and interfacial engineering, contributing to the development of safer, more efficient next generation solid-state batteries.

1. Introduction

Lithium metal batteries (LMBs) have garnered significant attention to meet the growing demand for efficient and sustainable energy storage systems as they offer high theoretical energy density.[1–3] However, due to the use of traditional liquid electrolytes, LMBs suffer from flammability, dendrite induced short circuits, and limited electrochemical stability[4–7] To overcome these limitations, solid-state electrolytes (SEs) have been widely investigated as they offer improved safety, increased energy density, and the ability to use lithium metal anodes.[8–12]

Garnet-based systems, such as LLZO, are among the most promising candidates for solid-state lithium batteries due to their superior thermal and chemical stability, high ionic conductivity, and wide electrochemical window.[13,14] Nevertheless, the practical implementation LLZO faces significant challenges when paired with Li metal anode. The lithiophobic nature of the surface of LLZO leads to poor wettability, resulting in high interfacial resistance and non-uniform Li deposition.[15] These interfacial issues not only affect the charge transfer efficiency but also leads to Li dendrite formation, thus reducing the cycling stability of the cells.[15–17] Hence, interface engineering should be carried out deeply to uncover the full potential of garnet-based SSEs for solid batteries.

In the literature, various interface strategies to reduce interfacial resistance (area specific

View Article Online
DOI: 10.1039/D5EB00026B

resistance, ASR) and improve the compatibility of garnet-based solid electrolytes with Li metal anodes have been explored. Metallic coatings, such as Au, Al, and Si, have been widely applied to improve wetting at the interface, achieving ASR values as low as ~50–150 $\Omega \cdot cm^2$.[18–20] These coatings enhance Li contact with the garnet surface and facilitate ionic transport across the interface. Similarly, Li-based interlayers, such as Li_3PO_4 and LiF, have been employed to further reduce interfacial resistance by promoting better ionic conductivity and suppressing interfacial reactions.[21,22] Chemical surface treatments have also been utilized to modify the surface energy of LLZO, improving wetting and ensuring a more uniform interface.[23,24]. Polymeric interlayers, including polyethylene oxide (PEO) based films, have been explored as well, serving as an intermediate layer that bridges the gap between the garnet electrolyte and lithium metal.[25,26] These polymeric films enhance adhesion and improve the mechanical compatibility of the interface, thereby addressing the contact issues between the two surfaces.

Despite the progress achieved with these strategies, significant challenges remain in addressing interfacial resistance and ensuring long term stability. Many approaches involve complex fabrication techniques or materials that are prone to degradation over extended cycling. Metallic coatings, for instance, often face reactivity issues with Li, compromising their stability. Although Li-based interlayers and polymeric films are initially effective, their limited compatibility with garnet surfaces and low ionic conductivity contribute to an increase in ASR over time. Chemical surface treatments, though beneficial for improving wetting, often lack reproducibility and can introduce impurities that degrade overall performance. These persistent issues highlight the difficulty of achieving a robust and stable interface that balances low ASR with practical scalability and reliability.

In this study, we propose an alternative approach of utilizing minimal amounts of liquid electrolytes (LEs) such as carbonate and ether-based liquid electrolytes to enhance the wettability and ionic conductivity at the LLZO/Li interface. Unlike complex deposition or treatment processes required for other strategies, the application of liquid electrolytes is straightforward, scalable, and cost effective. This study bridges the gap by examining the interfacial resistance and compatibility of LLZO with carbonate and ether-based LEs in symmetric cells, alongside its application in full cells with $LiFePO_4$ (LFP) cathodes. This approach bridges the physical gaps between the LLZO and Li, reducing interfacial resistance and ensuring uniform Li-ion transport, thereby suppressing dendrite growth and enhancing long term cycling stability. Ether-based electrolytes, in particular, demonstrate significant

View Article Online
DOI: 10.1039/D5EB00026B

advantages over conventional approaches, achieving an ASR as low as ~32 $\Omega \cdot cm^2$. These systems also exhibit a critical current density (CCD) of ~0.6 mA/cm^2, highlighting their ability to sustain high current densities without inducing dendrite formation, enabling stable long term cycling, maintaining over 1000 h of operation at 0.1 mA/cm^2, and delivering excellent capacity retention of 78.5% after 100 cycles with a Coulombic efficiency (CE) of 99.9% in full cells with LFP cathodes.

2. Experimental

Ga doped LLZO was synthesized via a solid state reaction method using the stoichiometric amounts of Li_2CO_3 (Soekawa Chemicals, 99.9%), La_2O_3 (High Purity Chemicals, 99.9%), ZrO_2 (Samchun Chemicals, 99.9%), and Ga_2O_3 (High Purity Chemicals, 99.9%). The precursors were ball milled in isopropanol for 24 h, with 5 wt% excess Li_2CO_3 added to compensate for lithium loss during sintering. The mixture was calcined at 850 °C for 6 h, ground, and further milled to achieve finer particle sizes. The resulting powder was pressed into pellets at 200 MPa using a cold isostatic press and sintered in air at 1200 °C for 6 h. The sintered pellets were polished and prepared for structural and electrochemical testing.

The structural properties were analyzed using X-ray diffraction (XRD, Rigaku) with Cu K_α over 2θ range of 10–70°, and Raman spectroscopy (NANOBASE Inc) with a 532 nm laser. Microstructural analysis was performed with a scanning electron microscope (Compact SEM SERON, AIS2000C). Li-ion conductivity was measured via electrochemical impedance spectroscopy (EIS) (Zurich Instruments MFIA) with a 20 mV AC signal over a frequency range of 1 Hz to 5 MHz and a temperature range of 5–65 °C. Symmetric Li|LLZO|Li cells were assembled in CR2032 type coin cells using minimal amounts of carbonate (1M $LiPF_6$ in EC/EMC (1:2 v/v) with 5 wt% FEC) or ether-based (1M LiTFSI in DOL/DME (1:1 v/v) with 2 wt% $LiNO_3$) LEs to ensure proper interfacial contact. The surface chemistry of LLZO/Li interface was examined using X-ray photoelectron spectroscopy (XPS, Scientific K-Alpha system, Thermo Scientific). Galvanostatic cycling tests were performed using a battery cycler (Won-A-Tech) to evaluate interfacial stability and long term performance at different current densities. Full Li|LLZO|LFP cells were fabricated with LFP cathodes prepared by coating a slurry of LFP, conductive carbon, and PVDF in an 8:1:1 weight ratio onto aluminum foil. Approximately 0.5 μL of ether-based LE was applied to improve interfacial contact on both sides of the LLZO pellets. The cells were heated at 60 °C for 24 h prior to testing and

View Article Online
DOI: 10.1039/D5EB00026B

subsequently evaluated at the same temperature under a 0.1 C charge/discharge rate.

3. Results and Discussion

Figure 1(a) shows the X-ray diffraction (XRD) pattern of Ga doped LLZO, compared with the standard diffraction pattern of cubic LLZO. The data confirm that LLZO crystallizes predominantly in the cubic garnet structure, as evidenced by the excellent alignment between the observed diffraction peaks and the standard cubic phase (PDF#97-026-1302). Key reflections such as (420), (332), and (422) are well defined, and no additional peaks corresponding to secondary phases, such as Ga_2O_3 or $La_2Zr_2O_7$ are detected. This indicates the successful incorporation of Ga into the garnet lattice without forming undesired byproducts. The sharp and symmetric diffraction peaks reflect the high crystallinity of the material, with no evidence of peak splitting associated tetragonal phase. This confirms that Ga doping effectively stabilizes the cubic structure by influencing the local environment of the lattice. Figure 1(b) presents the Raman spectroscopy data, further validating the cubic garnet structure.

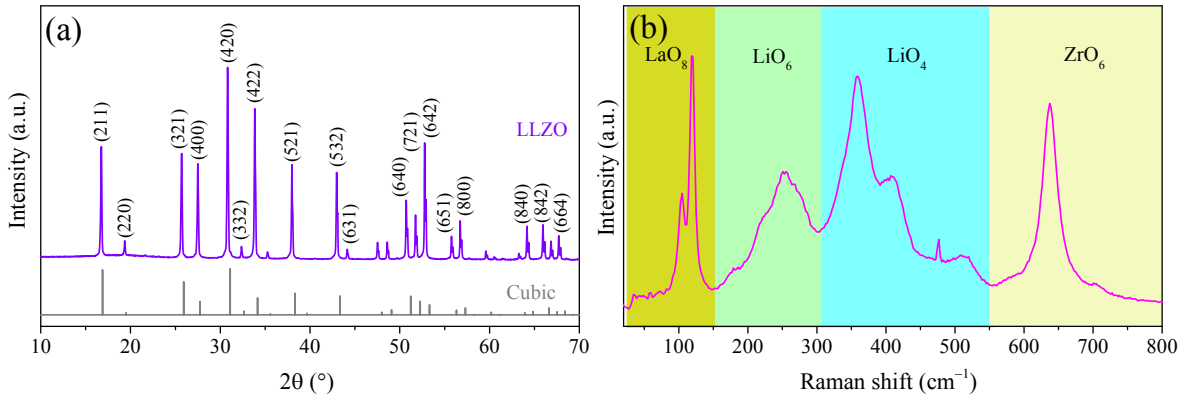

Figure 1. (a) XRD pattern of LLZO with standard cubic garnet phase confirming its cubic phase structure. (b) Raman spectrum further validating cubic phase formation.

The spectrum reveals characteristic vibrational modes of the cubic phase. Peaks in the low frequency region (150–200 cm^{-1}) correspond to La-O stretching vibrations within the garnet framework, while those in the mid frequency range (500–700 cm^{-1}) are assigned to Li-O stretching and bending vibrations, confirming the occupation of Li in the LLZO lattice.[27] Notably, no peaks indicative of secondary phases, such as carbonate or hydroxide species, are observed, emphasizing the high purity of the sample. Additionally, the absence of peak splitting

View Article Online
DOI: 10.1039/D5EB00026B

in the Raman spectrum supports the conclusion that Ga-doped LLZO adopts a pure cubic phase without any contribution from the tetragonal phase.[13,27] Thus, XRD and Raman spectroscopy confirm that Ga doping stabilizes the cubic LLZO structure and ensures the formation of a highly crystalline, phase pure material.

As shown in **Figure 2**(a), SEM reveals a dense and uniform microstructure for LLZO sintered at 1200 °C, with closely packed grains and negligible porosity, indicative of effective sintering. Such a dense microstructure reduces grain boundary resistance and improves mechanical properties, which are crucial for enhancing ionic conductivity. Elemental mappings shown in Figure 2(b-e) demonstrate the uniform distribution of La, Zr, and O, confirming their effective incorporation into the LLZO structure. However, Ga exhibits partial segregation along the grain boundaries, as seen in Figure 2(d). This behavior is commonly observed in Ga-doped LLZO and is attributed to liquid-phase-assisted sintering, where Ga promotes grain growth and enhances overall densification.[28,29] The EDS spectrum in Figure 2(f) further supports the presence of all constituent elements with distinct peaks corresponding to their characteristic energies. The relative atomic ratios of elements confirm the compositional integrity and phase purity of the synthesized material.

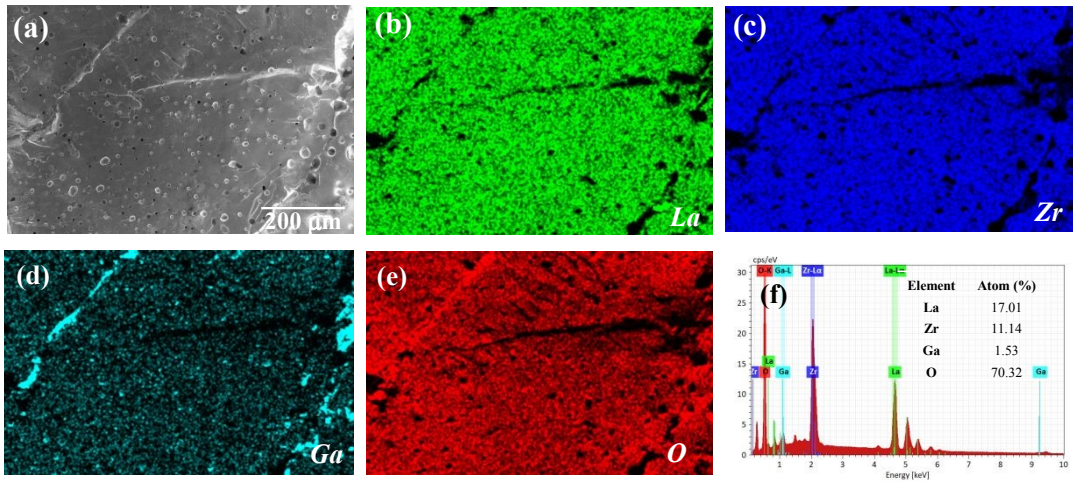

Figure 2. Microstructural and compositional properties of LLZO: (a) SEM image, (b-e) 2D maps of constituent elements, and (f) EDS spectrum showing the presence of La, Zr, Ga, and O.

Temperature dependent EIS is employed to get further insights into the electrochemical behavior of LLZO. **Figure 3**(a) represents the impedance behavior of LLZO at different temperatures, along with the equivalent circuit model used for fitting the data. The Nyquist plot

View Article Online
DOI: 10.1039/D5EB00026B

exhibits typical semi-circular arcs at higher frequencies, corresponding to the bulk (R_b) and grain boundary resistance (R_g), followed by a tail at lower frequencies associated with electrode polarization (R_{el}). The inset provides a zoomed view of the high frequency region, showing a highly depressed semicircle, which indicates indistinguishable contributions from bulk and grain boundary resistances. Therefore, the data has been simulated by equivalent circuit model consisting of two parallel RC circuits composed of R_t (total resistance of the pellet) and R_{el} resistance and CPE_t and CPE_{el} constant phase elements.[30] A good match was achieved between the experimental and simulated impedance patterns based on equivalent circuits, revealing a reduction in impedance with increasing temperature.

Figure 3(b) shows the temperature dependence of ionic conductivity (total) of LLZO. The conductivity was estimated from the following relation using dimensions of the pellet.

$$\sigma_{total}(T) = \sigma_0 e^{(-E_A/k_B T)} \quad (2)$$

where, σ_0 is a pre-exponential factor and T is the absolute temperature. E_a and k_B denote the activation energy and Boltzmann constant, respectively. The data show a linear relationship between log σ and 1/T, indicating thermally activated ionic transport governed by the Arrhenius equation. The calculated room temperature ionic conductivity is approximately 1.53 mS/cm, which competes with high value of conductivity reported for garnet-based solid electrolytes.[14,31–34] The observed low activation energy of 0.268 eV confirms an excellent mobility and thus efficient Li-ion transport through the Cubic LLZO.

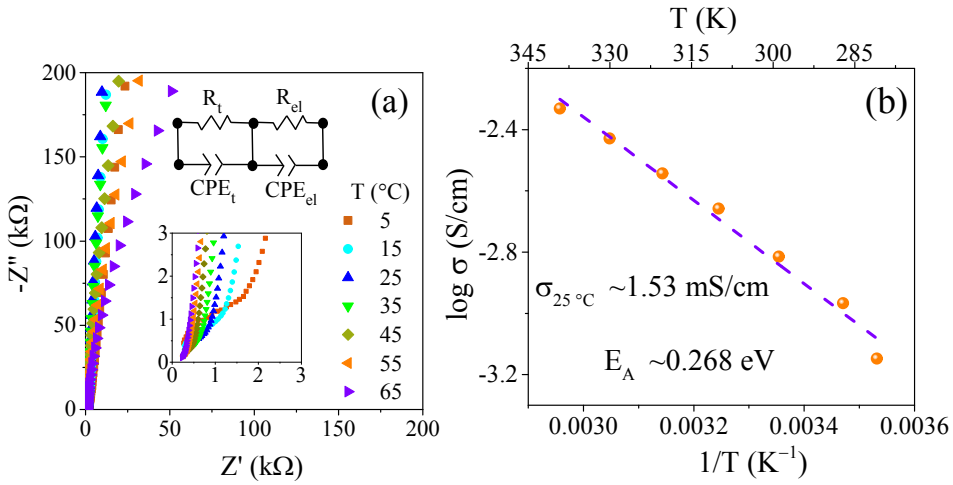

Figure 3. (a) Nyquist plot of impedance spectra measured at various temperatures, with a zoomed view and equivalent circuit model shown in the inset. (b) Arrhenius plot of temperature dependent ionic conductivity, indicating low activation energy.

View Article Online
DOI: 10.1039/D5EB00026B

EIS and cycling tests were conducted to systematically assess the impact of different LEs on the electrochemical performance of Li|LLZO|Li symmetric cells fabricated with LLZO as a SE (**Figure 4**). As shown in Figure 4a, the Nyquist plots reveal substantial differences depending on the LE used. To quantify the interfacial resistance, the impedance spectra were fitted using an equivalent circuit model comprising two parallel RC elements: R_{SE} and CPE_{SE}, representing the bulk and grain boundary resistance/capacitance of LLZO, and R_{int} and CPE_{int}, representing the interfacial resistance and non ideal capacitance at the LLZO/Li interface (inset, Figure 4a).[35,36] The ASR was extracted from the fitted interfacial resistance normalized to the electrode area. The cell assembled without any LE exhibited a significantly large semicircle (inset, Figure 4a). A very high ASR of ~39,800 Ω·cm^2 was observed, indicating a poor wetting at the LLZO/Li interface (Figure 4b). Upon incorporating LEs, the ASR dramatically decreased (Figure 4b). The cell utilizing the carbonate-based electrolyte showed a notable reduction to ~185 Ω·cm^2, suggesting improved wetting and enhanced Li-ion transport. However, the ether-based electrolyte demonstrated an even smaller semicircle, corresponding to an exceptionally

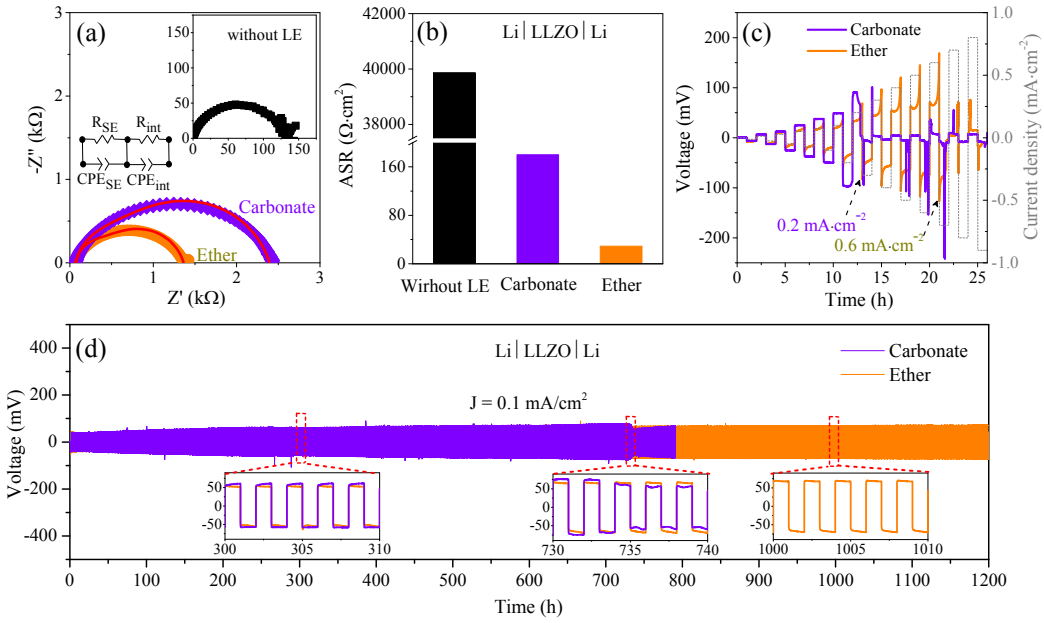

Figure 4. Electrochemical performance comparison of Li|LLZO|Li symmetric cells: (a) Nyquist plots along with equivalent RC circuits with and without LEs, (b) ASR values. Charge/discharge profiles (c) with increasing current density and (d) at 0.1 mA/cm^2 for carbonate and ether-based cells, with insets showing zoomed voltage profiles at selected time intervals.

low ASR of ~32 Ω·cm^2, highlighting superior interfacial contact and highly efficient ionic conduction across the LLZO/Li interface. These differences in ASR were further reflected in

View Article Online
DOI: 10.1039/D5EB00026B

CCD measurements (Figure 4c). The ether-based cell sustained a reasonably higher CCD of ~0.6 mA·cm^{-2}, whereas the carbonate-based cell failed at ~0.2 mA·cm^{-2}. The CCD achieved with the ether-based LE is relatively higher than values reported for many other strategies (~0.2–0.4 mA·cm^2).[37–40] The lower ASR of ether-based cells minimizes interfacial defects and current localization, promoting uniform lithium deposition and effectively suppressing dendrite growth. Long term cycling tests of Li|LLZO|Li symmetric cells at 0.1 mA/cm^2 and 60 °C further validated these findings (Figure 4d). The cell without any LE failed to operate even for one cycle (Figure S1b). This emphasizes the necessity of interfacial modification of LLZO. The carbonate-based symmetric cell initially exhibited reasonable cycling with an overpotential of ~61 mV; however, after ~730 h, a sudden voltage drop was observed (inset, Figure 4d). In sharp contrast, the ether-based cell maintained exceptionally stable voltage profiles with a consistently low overpotential (~58 mV) over 1000 h, confirming superior long term electrochemical stability. Furthermore, even under a higher current density of 0.2 mA/cm^2 (Figure S2), the ether-based cell demonstrated stable cycling for 300 h with average overpotential of ~70 mV, highlighting its excellent interfacial robustness.

To understand the origin of the observed interfacial stability, cross-sectional SEM and EIS analyses were conducted for symmetric cells assembled with and without LEs (**Figure 5**). Symmetric cells without any LE showed severe interfacial gaps and poor adhesion, resulting in rapid cell degradation **(**Figure S1**)**. Both carbonate and ether-based cells exhibited excellent interfacial contact before cycling, with no major morphological differences or degradation observed after extended cycling of 300 h (Figures 5a-d). This suggests that the application of a small amount of LE effectively improves and preserves the LLZO/Li interface. Although both carbonate and ether-based LES initially enhanced wettability, subsequent EIS analysis revealed that ASR increased for carbonate based cells with cycling, while ether-based systems exhibited negligible variation in impedance, maintaining superior interfacial stability during long term cycling (Figures 5e and 5f). These results align with the voltage stability trends observed in Figure 4d (Figure S3), reinforcing that strategic interfacial engineering with optimized electrolyte formulations is essential for achieving a stable LLZO/Li interface for durable LLZO-based lithium metal batteries.

View Article Online
DOI: 10.1039/D5EB00026B

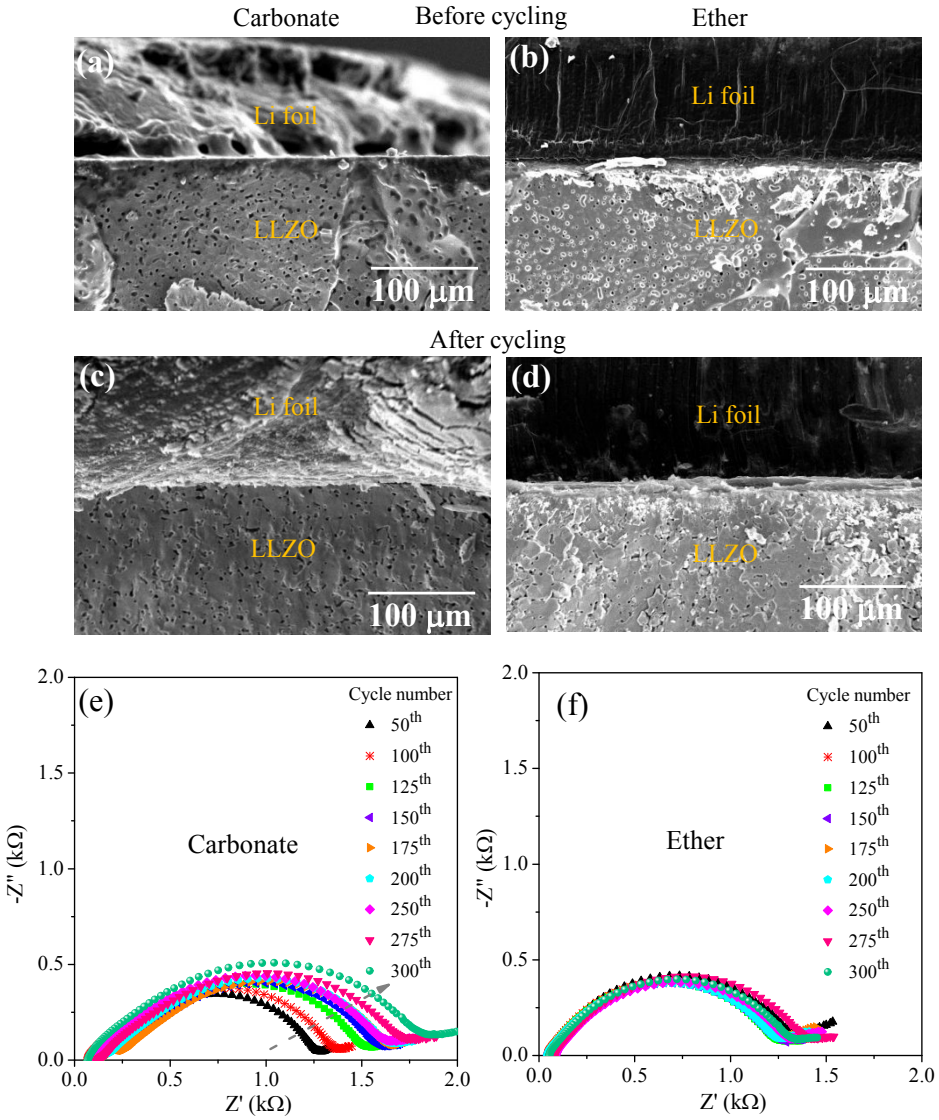

Figure 5. (a-d) Cross-sectional SEM and (e-f) impedance evolution of Li|LLZO|Li symmetric cells utilizing carbonate and ether based LEs with cycling.

To gain deeper insight into the interfacial chemistry/stability observed in symmetric cells with carbonate and ether-based LEs, high resolution XPS analysis was conducted on pristine LLZO and LLZO surfaces after LEs exposure (**Figure 6**). Spectra were recorded for F 1*s*, N 1*s*, and Li 1*s* core levels. Due to the high surface sensitivity of XPS and the small binding energy differences between various lithium containing species, peak deconvolution is challenging and often inconsistently reported in the literature.[35,41–46] Here, we carefully analyzed the F 1*s*, N 1*s*, and Li 1*s* spectra using CasaXPS software, considering the underlying materials chemistry. The F 1*s* spectrum showed no detectable signal for pristine LLZO (Figure 6a). Upon exposure

View Article Online
DOI: 10.1039/D5EB00026B

to the carbonate-based LE, three peaks were appeared at 685.4 eV, 686.9 eV, and 688.5 eV, corresponding to LiF, $Li_xPF_yO_z$, and CF_3 species, respectively (Figure 6d).[43,45] Ether-based LE treatment resulted in a single F 1*s* peak at 688.8 eV, attributed to CF_3 species from the decomposition of FSI or TFSI salts (Figure 6g). The N 1*s* spectrum revealed no signal for pristine or carbonate-treated LLZO (Figure 6b and e). However, the ether-treated sample showed two peaks at 399.5 eV and 400.9 eV, corresponding to Li_3N and LiN_xO_y, indicating the

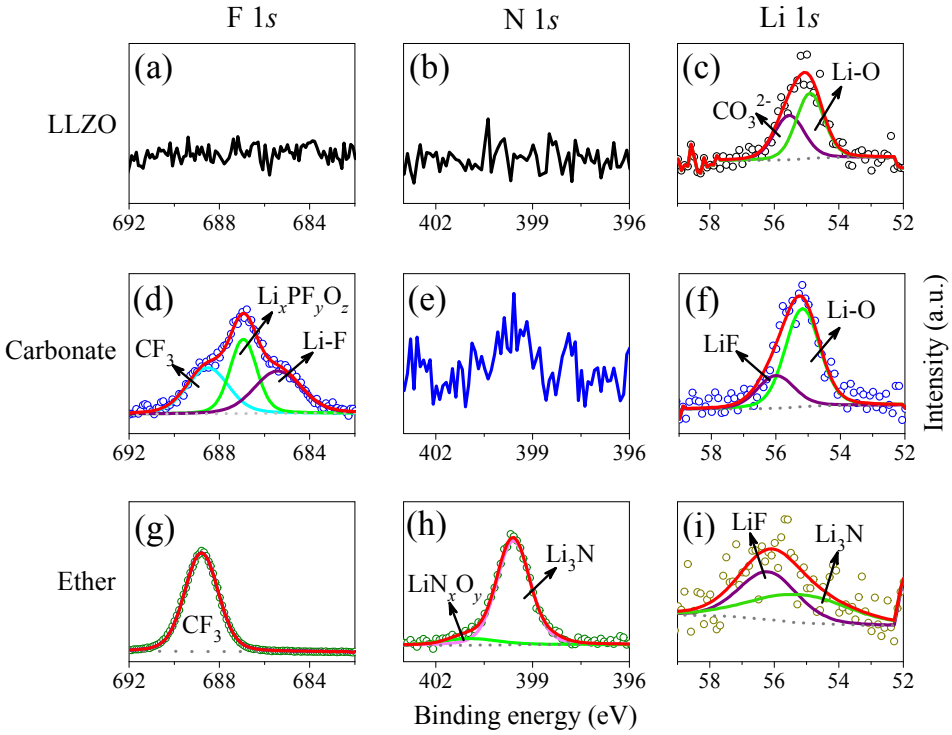

Figure 6. XPS spectra of LLZO before and after wetting with carbonate and ether-based LEs: (a) P 2*p*, (b) F 1*s*, (C) N 1*s*, (d) Li 1*s*.

formation of nitrogen rich interphases (Figure 6h).[47,48] The Li 1*s* region was often omitted or briefly discussed in many previous studies due to overlapping signal of Li_2O, LiOH, Li_2CO_3, LiF, $LiPF_6$, $Li_xPF_yO_z$.[49] In our case, the Li 1*s* spectrum of pristine LLZO exhibited two peaks centered at ~54.9 and 55.5 eV and eV, associated with Li–O (LLZO lattice) and Li_2CO_3 (Figure 6c).[50] For carbonate-treated LLZO, peaks were observed at the binding energies of ~ 55.1 and 56.0 eV. These were assigned to LLZO and LiF, respectively.[42,50] In case of ether-based system, peaks at ~55.2 and 56.2 eV, were ascribed to Li_3N and LiF, respectively (Figure 6i).[44,51] These XPS findings suggest that native Li_2CO_3 on the LLZO surface decomposes upon contact with

View Article Online
DOI: 10.1039/D5EB00026B

both electrolyte types, forming chemically distinct interphases. This was further supported by Fourier transform infrared spectroscopy (FTIR) analysis (Figure S4). Pristine LLZO exhibited two characteristic absorption bands at ~1430 cm^{-1} and ~850 cm^{-1}, which match well with carbonate groups of Li_2CO_3.[44,52] These bands disappeared after wetting with both carbonate and ether-based LEs and thermal treatment, confirming the Li_2CO_3 conversion into LiF, Li_3N, and $Li_xPF_yO_z$ depending on the electrolyte type.

To visualize the interfacial chemistry, schematic illustrations were developed (Figure 7). In the absence of LE, a substantial interfacial gap exists between Li metal and LLZO due to the presence of native Li_2CO_3, resulting in poor contact, high ASR, and immediate cell failure (Figure 7a). Carbonate-based LE react to form LiF and $Li_xPF_yO_z$ rich interphases (along with minor CF_3 species), reducing ASR and improving interface stability (Figure 7b). Ether-based systems form highly conductive interphases dominated by Li_3N and LiF (with minor CF_3 and LiN_xO_y species), leading to enhanced wetting, much lower ASR, higher critical current density, and excellent long term cycling performance (Figure 7c).

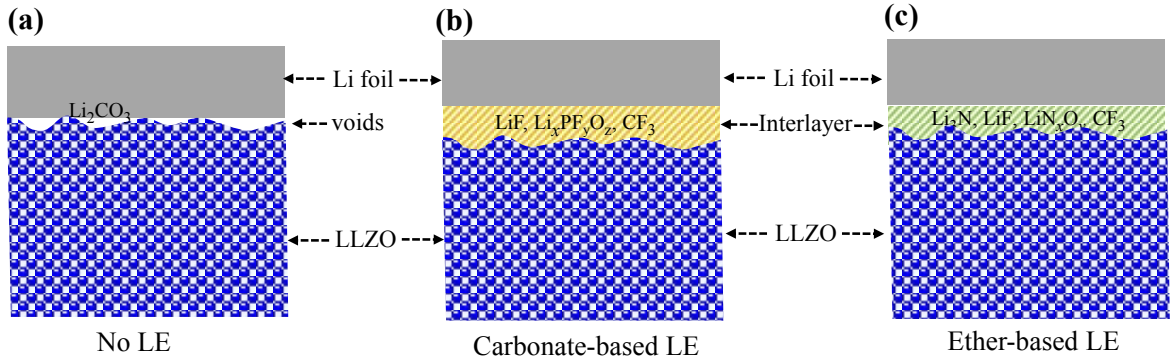

Figure 7. Schematic of LLZO/Li interfacial structures with and without LEs: (a) Poor contact without LE, (b) improved interfacial contact with carbonate-based LE, and (c) enhanced interfacial contact with ether-based LE, each forming different reaction products.

To assess the practical viability of the developed interfacial engineering strategy, Li|LLZO|LFP full cells were assembled using LLZO as the solid electrolyte, LFP as the cathode, and an ether-based LE to enhance interfacial wettability on both sides of the LLZO pellet (schematic shown in the inset of Figure 8a). Equivalent circuit modeling of the Nyquist plot reveals a low interfacial resistance of ~36 $\Omega \cdot cm^2$ and capacitance values in the range of 10^{-7} F, confirming efficient Li-ion transport and excellent compatibility at both the LLZO/Li and LLZO/LFP

View Article Online
DOI: 10.1039/D5EB00026B

interfaces (Figure 8a). The charge/discharge profiles at 0.1C exhibit highly stable voltage plateaus around 3.5 V, characteristic of the LFP redox couple, with minimal polarization and voltage hysteresis over 100 cycles (Figure 8b). As shown in Figure 8c, the full cell delivers an initial discharge capacity of ~127.4 mAh/g, gradually decreasing to ~100.3 mAh/g after 100 cycles, corresponding to a capacity retention of 78.5%. This moderate capacity fade reflects good durability for a hybrid solid-state system. Moreover, the CE remains exceptionally high (~99.9%) throughout cycling, indicating minimal parasitic reactions and excellent reversibility. In contrast, the full cell utilizing a carbonate-based LE exhibited significantly poorer capacity retention and unstable cycling performance (Figure S5). These results clearly demonstrate that the strategic use of ether-based LE enables long term cycling stability and reliable electrochemical performance in LLZO-based hybrid solid-state batteries.

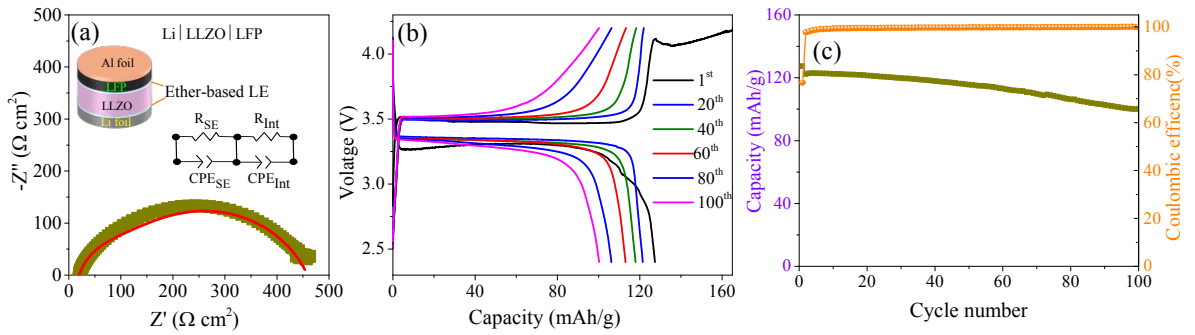

Figure 8. Electrochemical performance of the Li|LLZO|LFP full cell with ether-based LE. (a) Nyquist plot showing low interfacial resistance, with the full cell configuration depicted in the inset. (b) Charge/discharge voltage profiles at a 0.1C rate for selected cycles. (c) Cycling performance of the full cell.

4. Conclusion

The interfacial compatibility of cubic phase, highly conductive, and densely sintered LLZO was systematically investigated using minimal amounts of carbonate and ether-based LEs. Carbonate-based cells exhibited high interfacial resistance 185 $\Omega \cdot cm^2$ and a low critical current density 0.2 $mA \cdot cm^{-2}$ limiting their electrochemical performance. In contrast, ether-based systems significantly reduced interfacial resistance to 32 $\Omega \cdot cm^2$ and achieved a higher CCD 0.6 $mA \cdot cm^{-2}$, attributed to the formation of a stable Li_3N/LiF rich interphase. As a result, ether-based symmetric cells showed outstanding long term stability for over 1000 h with a

View Article Online
DOI: 10.1039/D5EB00026B

consistently low overpotential of 58 mV. Full cell tests further confirmed the compatibility and stability of LLZO with ether-based systems, achieving 78.5% capacity retention and 99.9% Coulombic efficiency over extended cycling. These findings emphasize the potential of minimal LE usage to optimize SE/electrode interfaces, for scalable and high performance next generation battery technologies.

Author contributions

Mohammad Nasir led methodology, experimental work, data collection, investigation, analysis, validation, and original draft writing. Jun Seo assisted in experimental work and draft review. Seo In Jung contributed to data collection and validation. Hee Jung Park supervised the project, handled conceptualization, project administration, funding, communication, and draft review.

Data availability

All data supporting the findings of this study are included in this article

Conflicts of interest

There are no conflicts to declare.

Acknowledgements

This research was supported by the National Research Foundation (NRF) of Korea, funded by the Government of Korea (MSIT) (Research project number: RS-2023-00236572). We thank Prof. J. Liu's members for valuable discussion.

References

1 M. Wan, R. Gilles, J. Vacik, H. Liu, N. L. Wu, S. Passerini and D. Bresser, *Small*, 2024, **20**, 2404437.

2 M. Gao, H. Li, L. Xu, Q. Xue, X. Wang, Y. Bai and C. Wu, *Journal of Energy Chemistry*, 2021, **59**, 666–687.

3 S. Zhang, R. Li, N. Hu, T. Deng, S. Weng, Z. Wu, D. Lu, H. Zhang, J. Zhang, X. Wang, L. Chen, L. Fan and X. Fan, *Nature Communications 2022 13:1*, 2022, **13**, 1–12.

4 X. Liu, A. Mariani, H. Adenusi and S. Passerini, *Angewandte Chemie International Edition*, 2023, **62**, e202219318.

View Article Online
DOI: 10.1039/D5EB00026B

5 Z. Huang, Z. Xiao, R. Jin, Z. Li, C. Shu, R. Shi, X. Wang, Z. Tang, W. Tang and Y. Wu, *Energy Environ Sci*, 2024, **17**, 5365–5386.

6 B. Khan, M. Nasir, J.-W. Lee, H. Jung and H. J. Park, *Batter Supercaps*, 2025, e202500227.

7 J. S. Park, M. Nasir, D. Kim, H. M. Jeong and H. J. Park, *Batter Supercaps*, 2025, e202400741.

8 M. Nasir, J. Seo, J. S. Park, S. I. Jung, H. J. Kim and H. J. Park, *Ceramist*, 2024, **27**, 1–8.

9 S. Kim, J. S. Kim, L. Miara, Y. Wang, S. K. Jung, S. Y. Park, Z. Song, H. Kim, M. Badding, J. M. Chang, V. Roev, G. Yoon, R. Kim, J. H. Kim, K. Yoon, D. Im and K. Kang, *Nat Commun*, DOI:10.1038/s41467-022-29531-x.

10 S. I. Jung, M. Nasir and H. J. Park, *ACS Appl Energy Mater*, DOI:10.1021/ACSAEM.5C00907/ASSET/IMAGES/LARGE/AE5C00907_0005.JPEG.

11 S. I. Jung, M. Nasir and H. J. Park, *J Mater Chem A Mater*, 2025, **13**, 4624–4633.

12 J. Seo, M. Nasir and H. J. Park, *ACS Appl Energy Mater*, 2025, **8**, 1518–1525.

13 M. Nasir, J. Seo, J. S. Park and H. J. Park, *J Eur Ceram Soc*, 2024, **44**, 4606–4611.

14 M. Nasir, J. Y. Park, P. Heo, K. H. Choi and H. J. Park, *Adv Funct Mater*, 2023, **33**, 2303397.

15 C. Zhu, T. Fuchs, S. A. L. Weber, F. H. Richter, G. Glasser, F. Weber, H. J. Butt, J. Janek and R. Berger, *Nat Commun*, 2023, **14**, 1–14.

16 J. Gao, J. Zhu, X. Li, J. Li, X. Guo, H. Li, W. Zhou, J. Gao, J. Zhu, X. Li, J. Li, X. Guo and H. Li, 2021, **31**, 2001918.

17 Z. Ning, G. Li, D. L. R. Melvin, Y. Chen, J. Bu, D. Spencer-Jolly, J. Liu, B. Hu, X. Gao, J. Perera, C. Gong, S. D. Pu, S. Zhang, B. Liu, G. O. Hartley, A. J. Bodey, R. I. Todd, P. S. Grant, D. E. J. Armstrong, T. J. Marrow, C. W. Monroe and P. G. Bruce, *Nature*, 2023, **618**, 287–293.

18 W. Luo, Y. Gong, Y. Zhu, K. K. Fu, J. Dai, S. D. Lacey, C. Wang, B. Liu, X. Han, Y. Mo, E. D. Wachsman and L. Hu, *J Am Chem Soc*, 2016, **138**, 12258–12262.

19 K. K. Fu, Y. Gong, B. Liu, Y. Zhu, S. Xu, Y. Yao, W. Luo, C. Wang, S. D. Lacey, J. Dai, Y. Chen, Y. Mo, E. Wachsman and L. Hu, *Sci Adv*, DOI:10.1126/SCIADV.1601659/SUPPL_FILE/1601659_SM.PDF.

20 G. V. Alexander, S. Patra, S. V. Sobhan Raj, M. K. Sugumar, M. M. Ud Din and R. Murugan, *J Power Sources*, 2018, **396**, 764–773.

21 J. Tang, Y. Niu, Y. Zhou, S. Chen, Y. Yang, X. Huang and B. Tian, *ACS Appl Mater Interfaces*, 2023, **15**, 5345–5356.

22 Z. Pan, S. Cao, X. Lu, G. Zhang, Q. Shen, C. Mao, X. Dai and F. Chen, *J Mater Chem A Mater*, 2023, **11**, 20676–20685.

23 A. Sharafi, E. Kazyak, A. L. Davis, S. Yu, T. Thompson, D. J. Siegel, N. P. Dasgupta and J. Sakamoto, *Chemistry of Materials*, 2017, **29**, 7961–7968.

24 R. Inada, S. Yasuda, H. Hosokawa, M. Saito, T. Tojo and Y. Sakurai, *Batteries 2018, Vol. 4, Page 26*, 2018, **4**, 26.

25 X. Liu, Z. Xiao, H. Peng, D. Jiang, H. Xie, Y. Sun, S. Zhong, Z. Qian and R. Wang, *Chem Asian J*, 2022, **17**, e202200929.

26 S. Li, J. Wang, F. Ji, M. Wang, Z. Hu, S. Huo, S. Zhang, H. Cheng and Y. Zhang, *J Power Sources*, 2024, **592**, 233969.

27 T. Thompson, J. Wolfenstine, J. L. Allen, M. Johannes, A. Huq, I. N. David and J. Sakamoto, *J Mater Chem A Mater*, 2014, **2**, 13431–13436.

28 D. Kim, M. H. Nguyen, S. H. Chun, J. Jeon, B. K. Kim and S. Park, *Int J Energy Res*, 2024, **2024**, 9050890.

View Article Online
DOI: 10.1039/D5EB00026B

29 W. Jeong, S. S. Park, J. Yun, H. R. Shin, J. Moon and J. W. Lee, *Energy Storage Mater*, 2023, **54**, 543–552.

30 X. Zhang, C. Li, W. Liu, T. S. Oh and J. W. Fergus, *Solid State Ion*, 2021, **369**, 115713.

31 D. Rettenwander, G. Redhammer, F. Preishuber-Pflügl, L. Cheng, L. Miara, R. Wagner, A. Welzl, E. Suard, M. M. Doeff, M. Wilkening, J. Fleig and G. Amthauer, *Chemistry of Materials*, 2016, **28**, 2384–2392.

32 R. Wagner, G. J. Redhammer, D. Rettenwander, A. Senyshyn, W. Schmidt, M. Wilkening and G. Amthauer, *Chemistry of Materials*, 2016, **28**, 1861–1871.

33 X. Tao, L. Yang, J. Liu, Z. Zang, P. Zeng, C. Zou, L. Yi, X. Chen, X. Liu and X. Wang, *J Alloys Compd*, 2023, **937**, 168380.

34 X. Huang, T. Xiu, M. E. Badding and Z. Wen, *Ceram Int*, 2018, **44**, 5660–5667.

35 S. A. Pervez, G. Kim, B. P. Vinayan, M. A. Cambaz, M. Kuenzel, M. Hekmatfar, M. Fichtner and S. Passerini, *Small*, 2020, **16**, 2000279.

36 M. Naguib, A. Sharafi, E. C. Self, H. M. Meyer, J. Sakamoto and J. Nanda, *ACS Appl Mater Interfaces*, 2019, **11**, 42042–42048.

37 Y. Li, X. Chen, A. Dolocan, Z. Cui, S. Xin, L. Xue, H. Xu, K. Park and J. B. Goodenough, *J Am Chem Soc*, 2018, **140**, 6448–6455.

38 X. He, F. Yan, M. Gao, Y. Shi, G. Ge, B. Shen and J. Zhai, *ACS Appl Mater Interfaces*, 2021, **13**, 42212–42219.

39 J. Wen, Y. Huang, J. Duan, Y. Wu, W. Luo, L. Zhou, C. Hu, L. Huang, X. Zheng, W. Yang, Z. Wen and Y. Huang, *ACS Nano*, 2019, **13**, 14549–14556.

40 T. Panneerselvam, R. Murugan and O. V. Sreejith, *ACS Appl Energy Mater*, 2024, **7**, 1700–1709.

41 J. Liu, X. Gao, G. O. Hartley, G. J. Rees, C. Gong, F. H. Richter, J. Janek, Y. Xia, A. W. Robertson, L. R. Johnson and P. G. Bruce, *Joule*, 2020, **4**, 101–108.

42 J. Leng, H. Wang, Y. Li, Z. Xiao, S. Wang, Z. Zhang and Z. Tang, *Appl Surf Sci*, 2022, **575**, 151638.

43 P. Jiang, J. Cao, B. Wei, G. Qian, S. Wang, Y. Shi, G. Du, X. Lu, C. Ouyang, F. Cao and X. Lu, *Energy Storage Mater*, 2022, **48**, 145–154.

44 N. Chen, B. Gui, B. Yang, C. Deng, Y. Liang, F. Zhang, B. Li, W. Sun, F. Wu and R. Chen, *Small*, 2024, **20**, 2305576.

45 Y. Guo, S. Pan, X. Yi, S. Chi, X. Yin, C. Geng, Q. Yin, Q. Y. Zhan, Z. Zhao, F. M. Jin, H. Fang, Y. B. He, F. Kang, S. Wu and Q. H. Yang, *Advanced Materials*, 2024, **36**, 2308493.

46 S. Sarkar, B. Chen, C. Zhou, S. N. Shirazi, F. Langer, J. Schwenzel and V. Thangadurai, *Adv Energy Mater*, 2023, **13**, 2203897.

47 Y. Liang, W. Wu, D. Li, H. Wu, C. Gao, Z. Chen, L. Ci and J. Zhang, *Adv Energy Mater*, 2022, **12**, 2202493.

48 B. Liu, Y. Zhang, Z. Wang, C. Ai, S. Liu, P. Liu, Y. Zhong, S. Lin, S. Deng, Q. Liu, G. Pan, X. Wang, X. Xia and J. Tu, *Advanced Materials*, 2020, **32**, 2003657.

49 A. M. Tripathi, W. N. Su and B. J. Hwang, *Chem Soc Rev*, 2018, **47**, 736–851.

50 W. Xia, B. Xu, H. Duan, Y. Guo, H. Kang, H. Li and H. Liu, *ACS Appl Mater Interfaces*, 2016, **8**, 5335–5342.

51 Y. X. Wang, S. K. Hong, H. P. Hsu and C. W. Lan, *Adv Mater Technol*, 2024, **9**, 2400116.

52 V. Janakiraman, M. Savio, A. N. Alodhayb, M. Muthuramamoorthy, M. Ammal Dhanalakshmi, M. Vimalan, M. Durai and K. Ganesh Kumar, *Journal of Materials Science: Materials in Electronics*, 2025, **36**, 1–16.

View Article Online
DOI: 10.1039/D5EB00026B

Data Availability Statement

The data that support the findings of this study are available from the corresponding author upon reasonable request.

Declaration of competing interest:

The authors declare that they have no known competing financial interests or personal relationships that could have appeared to influence the work reported in this paper.